




Article

Novel Mononuclear Tetrabromonitrosylrhenate(II) Complexes Containing Azole-Type Ligands: Magnetostructural Characterization through Hirshfeld Surfaces Analysis

Mario Pacheco ^{1,*} , Javier González-Platas ² , Carlos Kremer ¹ , Miguel Julve ³, Francesc Lloret ^{3,*} and Alicia Cuevas ¹

¹ Área de Química Inorgánica, Departamento Estrella Campos, Facultad de Química, Universidad de la República, Av. General Flores 2124, Montevideo CP 11800, Uruguay; acuevas@fq.edu.uy (A.C.)

² Departamento de Física, Instituto Universitario de Estudios Avanzados en Física Atómica, Molecular y Fotónica (IUDEA), MALTA Consolider Team, Universidad de La Laguna, Avenida Astrofísico Fco. Sánchez s/n, E-38204 La Laguna, Tenerife, Spain

³ Instituto de Ciencia Molecular (ICMol)-Departamento de Química Inorgánica, Universidad de Valencia, C/Catedrático José Beltrán 2, 46980 Paterna, Valencia, Spain; miguel.julve@uv.es

* Correspondence: mpacheco@fq.edu.uy (M.P.); francisco.lloret@uv.es (F.L.)

Abstract: Our research group has made incursions into the scarcely known coordination chemistry of rhenium(II). The literature shows that Re(II) mononuclear complexes are attractive in molecular magnetism due to high magnetic anisotropy because of a significant spin-orbit coupling, making them a potential source for new molecule-based magnets. In this work, we present the preparation of four novel Re(II) compounds of general formula $\text{NBu}_4[\text{Re}(\text{NO})\text{Br}_4(\text{L})]$ [NBu_4^+ = tetra-*n*-butylammonium; L = imidazole (1), pyrazole (2), 1,2,4-triazole (3) and 1H-tetrazole (4)]. The four compounds were fully characterized by single-crystal X-ray diffraction, infrared spectroscopy, and cryomagnetic measurements in the temperature range of 1.8–300 K. Their crystal structures consist of mononuclear $[\text{Re}(\text{NO})\text{Br}_4(\text{L})]^-$ complex anions and NBu_4^+ cations. Each Re(II) ion is six-coordinate with a linear nitrosyl group and one monodentate nitrogen-donor (L), which are trans-positioned, plus four bromide groups, building a tetragonally distorted octahedral surrounding. The inter-anionic contacts were thoroughly analyzed using Hirshfeld surface analyses (plots over the d_{norm} , shape index, and 2D fingerprints). Cryomagnetic measurements show that these complexes behave as quasi-magnetically isolated spin doublets with weak antiferromagnetic interactions at low temperatures. The magnetic behavior of Re(II) was modeled by the influence of the ligand field, tetragonal distortion, spin-orbit coupling, and covalence effects. In addition, the antiferromagnetic exchange coupling was correlated to the nature of the intermolecular interactions.

Keywords: X-ray structure; rhenium(II); triazole; pyrazole; imidazole; tetrazole; magnetic properties



Citation: Pacheco, M.; González-Platas, J.; Kremer, C.; Julve, M.; Lloret, F.; Cuevas, A. Novel Mononuclear Tetrabromonitrosylrhenate(II) Complexes Containing Azole-Type Ligands: Magnetostructural Characterization through Hirshfeld Surfaces Analysis. *Crystals* **2023**, *13*, 658. <https://doi.org/10.3390/cryst13040658>

Academic Editor: Waldemar Maniukiewicz

Received: 24 March 2023

Revised: 5 April 2023

Accepted: 6 April 2023

Published: 11 April 2023



Copyright: © 2023 by the authors. Licensee MDPI, Basel, Switzerland. This article is an open access article distributed under the terms and conditions of the Creative Commons Attribution (CC BY) license (<https://creativecommons.org/licenses/by/4.0/>).

1. Introduction

In the last twelve years, mononuclear rhenium(II) complexes have garnered interest due to their various properties, such as catalysis [1,2], substance delivery [3], and photochemistry [4]. In the field of molecular magnetism, the Re(II) ion's high anisotropy, resulting from significant spin-orbit coupling, makes its complexes a potential source for discovering new molecule-based magnets [5,6]. In this respect, an illustrative example is the single-molecule magnet (SMM) behavior reported for $[\{\text{MnCl}\}_4\{\text{Re}^{\text{II}}(\text{triphos})(\text{CN})_3\}_4]$ [triphos = 1,1,1-tris(diphenylphosphinomethyl)ethane] by Dunbar's group [7,8]. Since then, our research team has started a systematic magnetostructural study of new mononuclear rhenium(II) complexes containing potentially bridging diazine-type ligands that can generate polynuclear complexes [9–12]. Tetrabromonitrosylrhenate(II) complexes have proven themselves to be suitable metalloligands towards first-row transition metal ions whose

coordination sphere is partially blocked. The mononuclear Re(II) complexes behave like quasi-magnetically isolated spin doublets with weak antiferromagnetic interactions across short Re-X...X-Re intermolecular contacts. Some of these complexes have been studied as salts of small diamagnetic and paramagnetic ions, affecting the through-space magnetic coupling between the $[\text{Re}(\text{NO})\text{Br}_4(\text{L})]^-$ complex anions [13–15].

A detailed magnetic description of this type of compounds must be accompanied by a deep chemical characterization of the compound, particularly with regard to the electronic structure of the spin-carrying centers, their tridimensional arrangement, and connectivity, in order to formulate coherent Hamiltonian formalisms consistent with the number and type of metal centers in the crystal [16]. Herein, the observed magnetic exchange interactions occur in interionic or intermolecular forms. This behavior can be investigated through Hirshfeld surfaces analysis, which is a simple yet powerful tool that allows us to determine and describe semi-quantitatively the intermolecular surrounding in the considered species [17,18]. In this work, we focus on the preparation and characterization of a new set of Re(II) mononuclear complexes containing azole-type ligands that could potentially act as precursors of polynuclear compounds by using them as metalloligands [19–21]. Specifically, we report the synthesis, chemical, and cryomagnetic characterization of four novel compounds of $\text{NBu}_4[\text{Re}(\text{NO})\text{Br}_4(\text{L})]$ (NBu_4^+ = tetra-*n*-butylammonium; L = imidazole (1), pyrazole (2), 1,2,4-triazole (3) and 1*H*-tetrazole (4)). Additionally, we performed a detailed study of the crystal packing using Hirshfeld surfaces analysis and paid particular attention to the Br...Br contacts, π - π stacking, C-H...O, and conventional hydrogen bonds as potential pathways for through-space magnetic interactions [22].

2. Materials and Methods

2.1. Materials

All manipulations were performed under aerobic conditions, using materials as received (reagent grade). The precursor $\text{NBu}_4[\text{Re}(\text{NO})\text{Br}_4(\text{EtOH})]$ was prepared from KReO_4 and NO, as previously reported [9].

2.2. Physical Methods

Elemental analyses (C, H, N) were performed with a CE Instruments CHNS 1100 Elemental Analyzer [samples of 25 (1), 20 (2), 25 (3), and 23 mg (4)] by the Central Service for the Support to Experimental Research (SCSIE) at the University of Valencia. The IR spectra were recorded on an FTIR Shimadzu Prestige-21 spectrophotometer in the range 4000–400 cm^{-1} . In addition, magnetic susceptibility measurements were carried out on polycrystalline samples with a Superconducting Quantum Interference Design (SQUID) magnetometer in the 1.9–300 K temperature range. In order to avoid saturation phenomena, external dc magnetic fields of 250 G ($T < 50$ K) and 5000 G ($T \geq 50$ K) were used. Diamagnetic corrections from the constituent atoms were estimated from Pascal constants [23]. Corrections for the magnetization of the sample holder (a plastic bag) measured in the same conditions were also applied.

2.3. Synthesis of the Complexes

Complexes 1–4 were prepared by using a common synthetic procedure: 0.91 mmol of L was added to a solution of $\text{NBu}_4[\text{Re}(\text{NO})\text{Br}_4(\text{EtOH})]$ (0.060 mmol, 50 mg) dissolved in 20 cm^3 of EtOH. The reaction mixture was stirred at room temperature for three hours, leading to a yellow-greenish solution. Then, it was filtered to remove any small solid particles and allowed to evaporate slowly at room temperature. X-ray-quality crystals, as green polyhedrons, were grown after ten days. These were filtered off and dried in the air. Yield (based on Re): ca. 48 (1), 41 (2), 35 (3), and 41% (4). Calc. for $\text{C}_{19}\text{H}_{40}\text{Br}_4\text{N}_4\text{ORe}$ (1/2): C, 27.0; H, 4.76; N, 6.62. Found: C, 27.3; H, 4.85; N, 6.44% (1). C, 27.3; H, 4.76; N, 6.48% (2). Anal. Calc. for $\text{C}_{18}\text{H}_{39}\text{Br}_4\text{N}_5\text{ORe}$ (3): C, 25.5; H, 4.64; N, 8.26. Found: C, 25.2; H, 4.64; N, 8.26% (3). Anal. Calc. for $\text{C}_{17}\text{H}_{38}\text{Br}_4\text{N}_6\text{ORe}$ (4): C, 24.1; H, 4.51; N, 9.91. Found: C, 24.0;

H, 4.51; N, 9.91% (4). IR (KBr disk/cm⁻¹): $\nu(\text{NO})$ is located at 1765(s), 1769(s), 1769(s) and 1765(s) for 1–4, respectively. For other IR absorption bands, refer to Table S1 [24–26].

2.4. X-ray Data Collection and Structure Refinement

X-ray diffraction data were collected for single crystals of 1–4 using Agilent Super-NOVA (for 1, 2, and 4) and Bruker D8 venture (for 3) diffractometers at 150 K (for 1 and 3) and 293 K (for 2 and 4), with microfocus X-ray Mo K α radiation ($\lambda = 0.71073 \text{ \AA}$) used in both diffractometers. CrysAlisPro v2021 [27] software (1, 2, and 4) and Apex2 [28] (3) were employed to collect, index, scale, and apply a numerical absorption correction based on Gaussian integration over a multifaceted crystal model. The structures were solved by applying the dual-space algorithm implemented in the SHELXT-2014 program [29]. Fourier recycling and least-squares refinement were used for the model completion with SHELXL-2018 [30]. All non-hydrogen atoms were refined with anisotropic thermal parameters through full-matrix least-squares procedures on F^2 . All hydrogen atoms were allowed to ride on their parent atoms with $U_{\text{iso}}(\text{H}) = 1.2U_{\text{eq}}(\text{C})$. Geometrical analysis of the interactions in the structures was performed with PLATON [31] and Olex2 [32] programs. Only in structure 4 did we apply restraints to the C–C distances for one of the NBu_4^+ cations since it presented a slight disorder. The CIF files contain the corresponding refinement details. Crystal data, collection procedures, and refinement results are summarized in Table S2, while selected bond lengths and angles are listed in Table 1. Mercury software (2022.1.0 version) was used for crystal structure visualizations [33]. The crystallographic data for the structures reported in this paper have been deposited with the Cambridge Crystallographic Data Centre as supplementary publication 2247513–2247516. Copies of the data can be obtained free of charge by applying to the CCDC, Cambridge, UK (<http://www.ccdc.cam.ac.uk> (accessed on 6 April 2023)).

Table 1. Selected bond distances (\AA) and angles ($^\circ$) for 1–4.

	Bond Lengths (\AA)			
	1	2	3	4A/4B
Re1–N2 _L	2.173(4)	2.191(3)	2.194(4)	2.171(12)/2.183(12)
Re1–N1 _{NO}	1.736(4)	1.732(4)	1.743(4)	1.735(13)/1.759(14)
Re1–Br1	2.5628(5)	2.5335(5)	2.5558(5)	2.5013(16)/2.5020(18)
Re1–Br2	2.5347(5)	2.5346(5)	2.5290(4)	2.5197(17)/2.5286(18)
Re1–Br3	2.5103(5)	2.5250(5)	2.5041(4)	2.5172(15)/2.5017(13)
Re1–Br4	2.5274(5)	2.5130(5)	2.5228(5)	2.5145(16)/2.5070(16)
N1 _{NO} –O1	1.185(5)	1.176(5)	1.179(5)	1.139(13)/1.100(14)
	Bond angles ($^\circ$)			
N1 _{NO} –Re1–N2 _L	178.69(14)	177.6(1)	177.9(1)	178.8(5)/179.2(6)
Re1–N _{NO} –O1	177.8(4)	177.5(3)	176.8(3)	177.3(13)/177.6(16)
Br1–Re1–Br3	172.141(19)	173.98(2)	171.41(2)	171.11(6)/171.99(6)
Br2–Re1–Br4	175.197(18)	171.72(2)	173.71(2)	173.20(6)/172.77(7)
N1 _{NO} –Re1–Br2	90.93(12)	96.5(1)	94.1(1)	91.7(4)/93.0(4)
N2 _L –Re1–Br2	88.13(9)	85.87(9)	87.03(9)	87.3(3)/87.0(3)

2.5. Hirshfeld Surface Analysis

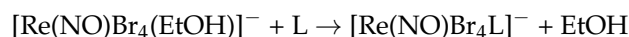
Hirshfeld surfaces [34] were constructed using the Crystal Explorer 17 software [35]. In particular, the intermolecular interactions in the solid state were studied by mapping the surface over the d_{norm} along with the two-dimensional fingerprint plots and over the shape index surface [36,37]. The Hirshfeld surfaces mapped over d_{norm} were calculated with the default setting of arbitrary units range; the rotation of the generated plot enables the identification of regions of interest. The colors employed to refer to the shortest and longest d_{norm} are red and blue, respectively. Red spots on the surface correspond to the shortest contacts within the surface, indicating the formation of intermolecular bonds. Contacts close in length to the van der Waals limit are white-colored [18]. Moreover,

2D fingerprint plots were computed for each interatomic contact and overall interaction. In the computation of individual interatomic contacts, the reciprocal interaction of each interatomic contact was also included.

3. Results

3.1. Details on the Preparation and Characterization of the Complexes

All of the complexes were prepared via ligand substitution from the anionic precursor $[\text{Re}(\text{NO})\text{Br}_4(\text{EtOH})]^-$ as shown in the following chemical equation:



This reactant complex has been previously used as a precursor for other tetrabromonitrosylrhenate(II) complexes [9,38]. The $\{\text{Re}(\text{NO})\text{Br}_4\}^-$ fragment appears to be highly stable. The ethanol ligand is an easy-leaving group upon its substitution by other nitrogen donors from aromatic ligands under mild conditions because of the trans effect produced by the NO group. Higher yields are achieved in the presence of an excess of the substituent ligand. The IR spectra of these metal complexes are dominated by the characteristic stretching mode of the nitrosyl group at approximately $1750\text{--}1770\text{ cm}^{-1}$. This absorption peak experiences a mild shift when the ligand substitution occurs, making it helpful in monitoring the ligand exchange in the aforementioned reaction.

3.2. Crystal Structure and Hirshfeld Analysis

Single crystals of **1–4** were grown directly from the reaction solution and were used for the X-ray data collection. We observed how **1–3** crystallize in the monoclinic crystal system, space group $P2_1/n$, whereas **4** crystallizes in the monoclinic space group $P2_1/c$. They consist of discrete $[\text{Re}(\text{NO})\text{Br}_4(\text{L})]^-$ complex anions and bulky $n\text{-(C}_4\text{H}_9)_4\text{N}^+$ organic cations in a 1:1 molar ratio, which are kept by electrostatic and van der Waals interactions.

Perspective views of the $[\text{Re}(\text{NO})\text{Br}_4(\text{L})]^-$ complex anion of **1–4** are presented in Figure 1, and the main bond lengths and angles are summarized in Table 1. Each $[\text{Re}(\text{NO})\text{Br}_4(\text{L})]^-$ unit comprises a rhenium(II) central ion surrounded by four bromide ligands in an equatorial plane, one NO group, and an azole-type ligand in the axial position. The geometry of the complex can be qualitatively described as a distorted octahedron and it is quantitatively confirmed by continuous symmetry measures (Table S3, [39]). The L ligands are coordinated to the rhenium(II) center through a nitrogen atom. The rhenium atom is slightly displaced from the mean equatorial plane towards the NO group, with the values of the $d(\text{Re}\text{--plane (centroid)})$ being equal to 0.138 (**1**), 0.156 (**2**), 0.161 (**3**), 0.171 (**4A**) and 0.166 Å (**4B**). The Re–NO group is practically linear, and the Re–N_{NO} and N–O distances agree with those previously observed in similar complexes [11,14] (see Table 1). The Re–Br bond lengths are comparable, covering the narrow range 2.5017–2.5628 Å, similar to previously reported values. The fact that the values of the Re1–Br1 bond distance observed in **1–3** are slightly longer than the other Re–Br bonds is due to the participation of Br1 in Br \cdots Br or Br \cdots H intermolecular contacts in their respective compounds, as we will analyze later in this work. The planarity of the L ligands in **1–4** is preserved upon coordination, and their C–C and C–N bond lengths are almost identical to those observed in the corresponding free molecules in the solid state.

The analysis of the crystal packing of the complex anions in **1–3** reveals a similar pattern between them. Infinite supramolecular chains of $[\text{Re}(\text{NO})\text{Br}_4(\text{L})]^-$ units are observed along the crystallographic *b*-axis, connected by bromo and hydrogen intermolecular contacts as well as π -stacking interactions [40,41], as shown in Figures 2, 3 and S2. These shortest intermolecular Br \cdots Br distances are 3.7387(6) (Br2 \cdots Br3ⁱ in **1**), 3.8811(7) (Br1 \cdots Br4ⁱ in **2**) and 3.7817(5) Å (Br4 \cdots Br3ⁱⁱ in **3** [symmetry code: (i) = $\frac{1}{2} - x, -\frac{1}{2} + y, \frac{1}{2} - z$; (ii) = $1.5 - x, -1/2 + y, 1.5 - z$]). They are slightly greater than the sum of the van der Waals radii (ca. 3.7 Å) [42–44] but considered in any matter as weak intermolecular contacts [45]. Additionally, π -stacking interactions [40] are observed between the pairs of HIm ligands in **1** [$d(\text{C}\cdots\text{C}) = 3.516\text{ \AA}$; $\angle\text{P_CC} = 27.171^\circ$], the Hpz ligands in **2** [$d(\text{C}\cdots\text{C}) = 3.910\text{ \AA}$;

$\langle P_CC = 31.97^\circ \rangle$ and the Htz ligands in **3** [$d(C\cdots C) = 3.677 \text{ \AA}$; $\langle P_CC = 30.72^\circ \rangle$, along the crystallographic b axis [$\langle P_CC$ is the slip angle between the normal of the pyridine plane (P) and the centroid vector (C)]. Finally, it is worth mentioning the observation of two weak hydrogen bonds in **1** between the Br1 and Br2 atoms from an anionic unit and the H3 and H2 atoms, respectively, from the imidazole ligand from another complex anion unit [the imidazole ligand from another complex anion unit [$d(\text{Br}1\cdots\text{H}3) = 2.7029 \text{ \AA}$; $d(\text{N}3\cdots\text{Br}1) = 3.531(4) \text{ \AA}$; $\langle(\text{N}3\text{--H}3\cdots\text{Br}1) = 161.97^\circ$; $d(\text{Br}2\cdots\text{H}2) = 3.0119 \text{ \AA}$; $d(\text{N}2\cdots\text{Br}2) = 3.678(5) \text{ \AA}$; $\langle(\text{C}2\text{--H}2\cdots\text{Br}2) = 129.88^\circ$]. Similar intermolecular hydrogen bonds are observed in **3** between Br1 and the H1 atom from the Htz ligand of an adjacent complex anion [$d(\text{Br}1\cdots\text{H}1) = 2.6246 \text{ \AA}$; $d(\text{C}1\cdots\text{Br}1) = 3.534(5) \text{ \AA}$; $\langle(\text{C}1\text{--H}1\cdots\text{Br}1) = 165.6^\circ$].

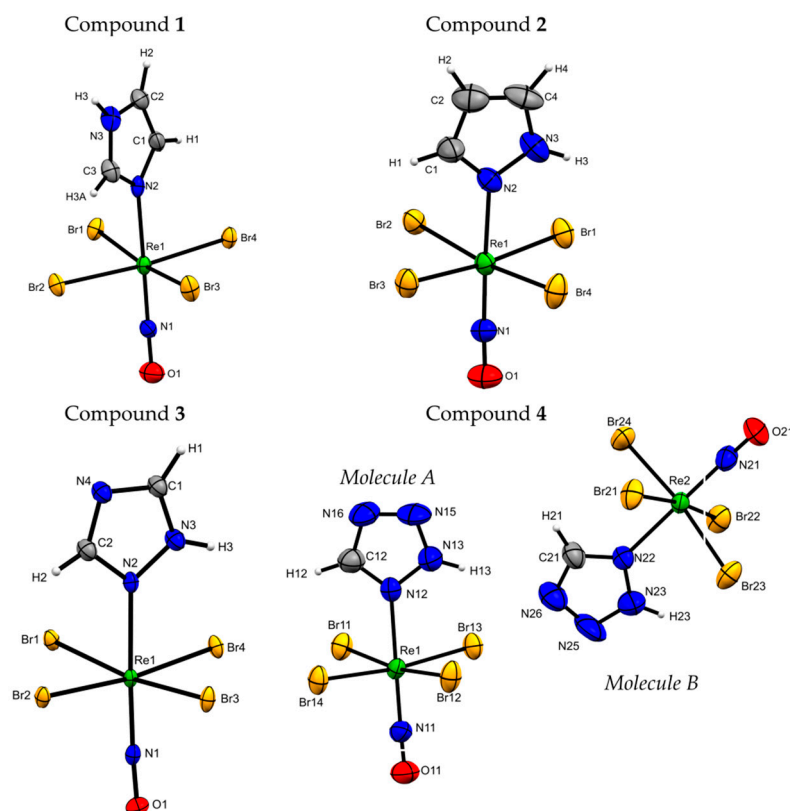


Figure 1. Perspective drawings of **1–4** showing the atom numbering. Thermal ellipsoids are plotted at a 30% probability level. The Bu_4N^+ cation was omitted for clarity. A and B stand for the two crystallographically independent complex anions in **4**.

The crystal packing in **4** shows a different pattern, as shown in Figure 3a. A supramolecular corrugated sheet parallel to the bc plane is formed through intermolecular N–H \cdots H hydrogen bonds and weak Br \cdots Br and Br \cdots N-type contacts. The hydrogen bonds correspond to the N13–H13 \cdots N26 set of atoms [$d(\text{N}26\cdots\text{H}13) = 2.55 \text{ \AA}$; $d(\text{N}13\cdots\text{N}26) = 3.41(2) \text{ \AA}$; $\langle(\text{N}13\text{--H}13\cdots\text{N}26) = 176^\circ$]. The Br \cdots Br contacts observed involve the Br11 and Br22ⁱⁱⁱ atoms [symmetry code: (iii) = $x, 1.5 - y, \frac{1}{2} + z$], the distance between them being $3.574(3) \text{ \AA}$, a value which is 3.4% smaller than the sum of the van der Waals radii. The Br \cdots N contacts concern the Br13 and N26^{iv} atoms [symmetry code: (iv) = x, y, z], the value of the interatomic distance being $3.32(2) \text{ \AA}$. The bulky NBu_4^+ cations separate these supramolecular 2D motifs from each other well, and no intermolecular interactions are observed between the anionic sheets. Furthermore, no π – π stacking is observed in the crystal structure. It is worth pointing out that the $[\text{Re}(\text{NO})\text{Br}_5\text{L}]^-$ anions are arranged similarly in **1–3**, that is, with all of the anionic units orientated antiparallel in the same direction, whereas the $[\text{Re}(\text{NO})\text{Br}_4(\text{Htrz})]^-$ complex anions display different orientations in the crystal of **4**, as shown in Figure 3b.

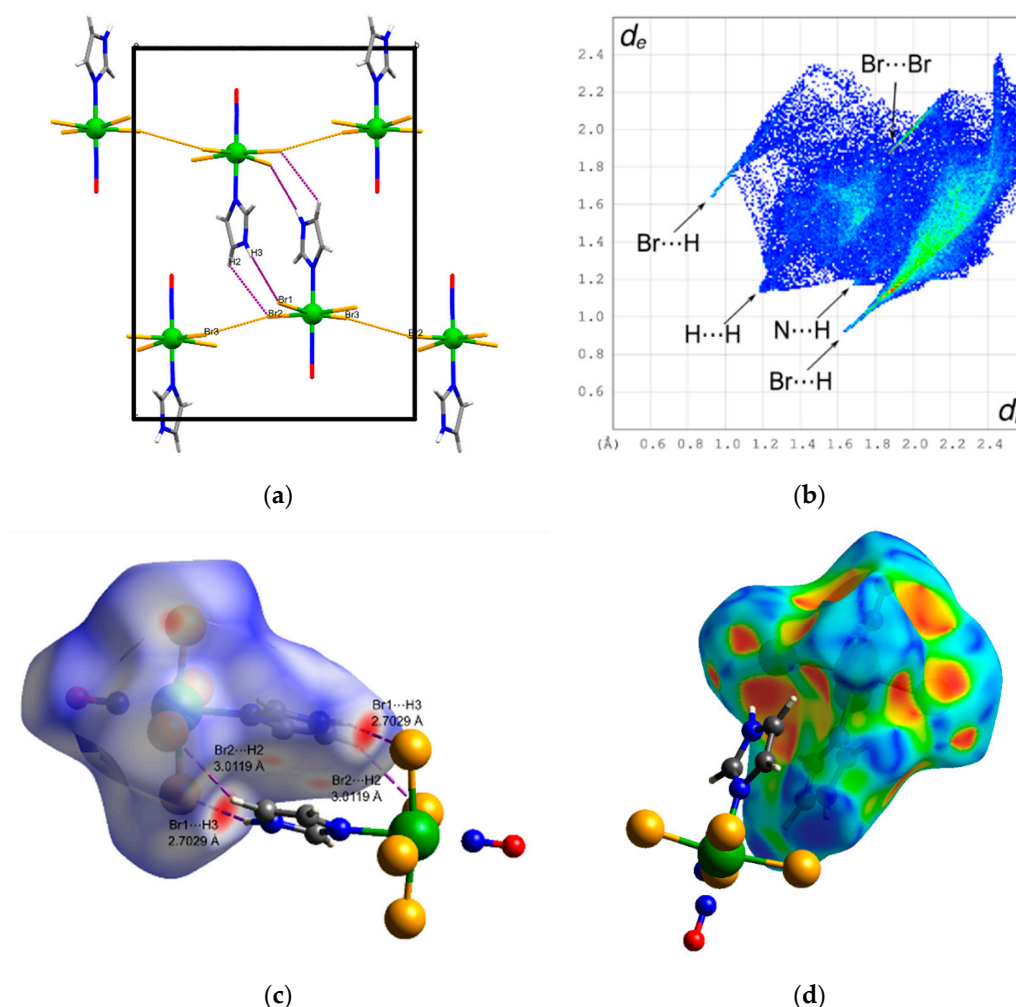


Figure 2. (a) Packing diagram down the crystallographic a axis, (b) fingerprint plot, (c) d_{norm} surface, and (d) shape index surface of the $[\text{Re}(\text{NO})\text{Br}_4(\text{HIm})]^-$ anionic units in **1**. Short Br \cdots Br (yellow), Br \cdots H (purple) contacts and π - π stacking interactions (grey ovals) are shown.

The crystal packing in **4** shows a different pattern, as shown in Figure 3a. A supramolecular corrugated sheet parallel to the bc plane is formed through intermolecular N-H \cdots H hydrogen bonds and weak Br \cdots Br and Br \cdots N-type contacts. The hydrogen bonds correspond to the N13-H13 \cdots N26 set of atoms [$d(\text{N}26\cdots\text{H}13) = 2.55 \text{ \AA}$; $d(\text{N}13\cdots\text{N}26) = 3.41(2) \text{ \AA}$; $\angle(\text{N}13\text{-H}13\cdots\text{N}26) = 176^\circ$]. The Br \cdots Br contacts observed involve the Br11 and Br22ⁱⁱⁱ atoms [symmetry code: (iii) = $x, 1.5 - y, \frac{1}{2} + z$], the distance between them being $3.574(3) \text{ \AA}$, a value which is 3.4% smaller than the sum of the van der Waals radii. The Br \cdots N contacts concern the Br13 and N26^{iv} atoms [symmetry code: (iv) = x, y, z], the value of the interatomic distance being $3.32(2) \text{ \AA}$. The bulky NBu_4^+ cations separate these supramolecular 2D motifs from each other well, and no intermolecular interactions are observed between the anionic sheets. Furthermore, no π - π stacking is observed in the crystal structure. It is worth pointing out that the $[\text{Re}(\text{NO})\text{Br}_5\text{L}]^-$ anions are arranged similarly in **1**–**3**, that is, with all of the anionic units orientated antiparallel in the same direction, whereas the $[\text{Re}(\text{NO})\text{Br}_4(\text{Htrz})]^-$ complex anions display different orientations in the crystal of **4**, as shown in Figure 3b.

In order to gain a deeper understanding of the intermolecular contacts between the complex anions in **1**–**4**, we conducted a Hirshfeld surface analysis on this family of compounds. While a direct inspection of the crystal structure usually reveals the intermolecular contacts, Hirshfeld surface analysis allows us to qualitatively correlate the strength of intermolecular contacts with the intensity of the red spots in the d_{norm} plots [46]. In **1** and

3, the strongest inter-anion interactions are due to Br–H contacts. However, no solid red spots due to anion–anion interactions are observed in the Hirshfeld surface over the d_{norm} in **2**. White-colored surface areas are present around the shortest Br···Br intermolecular distances in **1–3** due to the values relative to the sum of the van der Waals radii.

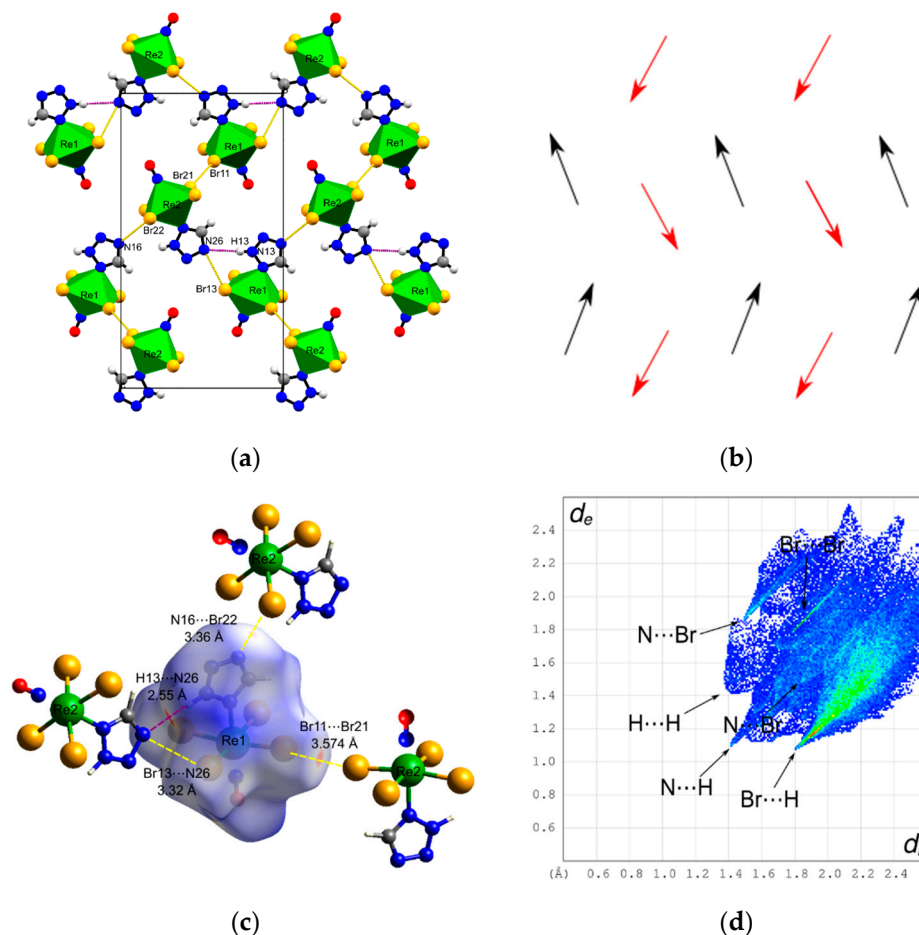


Figure 3. (a) Packing diagram down the crystallographic a axis; (b) complex anion orientation scheme along the crystallographic a axis (black and red arrows represent the A and B molecules, respectively); (c) d_{norm} surface and (d) shape index surface of the $[\text{Re}(\text{NO})\text{Br}_4(\text{Htrz})]^-$ units in **4**. Short through space Br···Br (yellow) and Br···N (yellow) contacts and N–H···N hydrogen bonds (purple) are also shown.

Conversely, the Hirshfeld plot over the d_{norm} map for **4A** reveals the presence of equally significant Br···Br and Br···N through space contacts and N–H···N hydrogen bonds. Notably, in contrast to what usually constitutes the focus of discussion, conventional hydrogen bonding often makes relatively small percentage contributions to the overall surface. The HS analysis of anion B in **4** reveals that the interaction for this molecule only varies in proportion (less than 1%) and not in nature, compared to the case of the A anion. In all compounds, the other red spots observed that we do not point out are due to less-significant cation–anion interactions (magnetically speaking). The supramolecular 2D fingerprint plots analysis shown in Figures 2, 3b, S2 and S3b, and the quantitative analysis of the contributions of the different intermolecular contacts to the HS of the anions shown in Figure 4, reveals that the main contribution to the HS is H-involving contacts, mainly Br···H (50% to 53%) and H···H contacts (11% to 22%). This is expected due to the bulky bromide ligands of the complex anion and the presence of the large NBu_4^+ cation. The exclusively anion–anion interactions (of magnetic interest) that contribute to the HS are the Br···N and Br···Br-type contacts. However, they contribute less than 5% and 3% to the total HS, respectively.

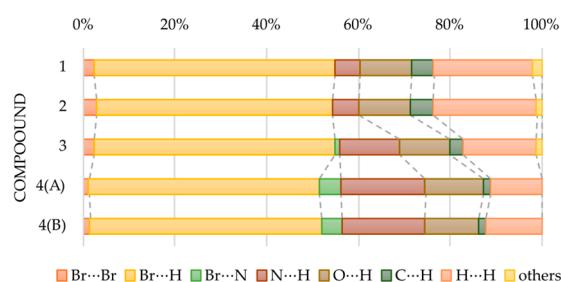


Figure 4. Relative contributions to the Hirshfeld surface area of the overall close molecular contacts for the complex anions in 1–4.

The HS surfaces plotted over the shape index [Figures 2, 3d, S2 and S3d] show triangular-shaped regions around the aromatic rings, indicating that $\pi \cdots \pi$ stacking interactions occur in the crystal packing. However, it is found that these stacking interactions are very weak because the values of the centroid-to-centroid separation range from 4.755(3) to 5.963(1) Å. This can also be seen as brighter regions near the center of the fingerprint plot, just in the vicinity of (d_i, d_e) 1.8–2.0 Å, a range of values typical of the interplanar spacing of polycyclic aromatic hydrocarbons.

3.3. Magnetic Properties

The temperature dependence of the $\chi_M T$ product per Re(II) ion for 1–4 is shown in Figure 5. A quasi-Curie law is observed in a wide range of temperatures with a $\chi_M T$ value around 0.43 cm³ K mol^{−1} at 295 K and a slight constant decrease in the $\chi_M T$ value, which is as expected for a local spin doublet ($S_{Re} = 1/2$) with a temperature-independent paramagnetism (TIP). However, upon cooling below c.a. 15 K, $\chi_M T$ decreases significantly due to the occurrence of antiferromagnetic interactions between the paramagnetic anionic units, the smallest value at 2.0 K being 0.207 cm³ mol^{−1} K for 2.

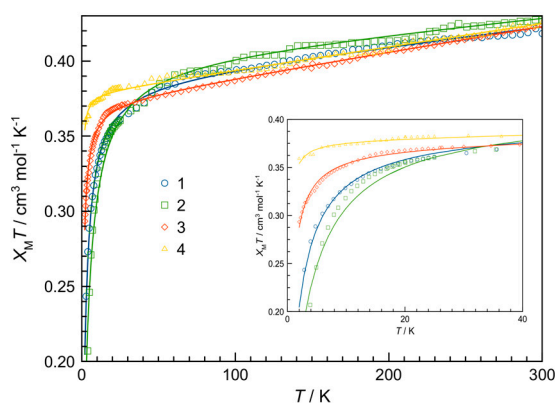


Figure 5. Thermal dependence of the $\chi_M T$ product for 1–4. The inset shows a detail of the low-temperature domain.

As previously reported, the theoretical magnetic behavior of magnetically non-interacting six-coordinate Re(II) complexes in an octahedral environment can be reproduced by considering a sequence of perturbations made up by the spin-orbit coupling (SOC), the tetragonal distortion, and the magnetic field [9,10]. Consequently, having in mind these considerations and the crystal structures of 1–4, their magnetic susceptibility data were analyzed through the following Hamiltonian [Equation (1)]:

$$\hat{H}_{Re} = k\lambda\hat{L}\hat{S} + \Delta\left(\hat{L}_z^2 - 2/3\right) + \beta H(k\hat{L} + g_e\hat{S}). \quad (1)$$

The first term in Equation (1) considers the spin-orbit coupling between the $S = 1/2$ spin and the $L = 1$ effective angular momentum for the 2T_2 ground term of Re(II) due to the

isomorphism $||T_2|| = -||P||$ [9,47]. λ is the spin-orbit coupling parameter, and κ is the orbital reduction factor. In the second term, Δ represents the energy gap between the 2E and 2B_2 levels arising from splitting the 2T_2 ground state in octahedral geometry (axial distortion) [48]. Finally, the last term accounts for the Zeeman effects, g_e being the Landé factor for the free electron. In the absence of SOC, the tetragonal distortion (considering the C_{4v} point group) splits the 2T_2 term into an orbital singlet (2B_2) and an orbital doublet (2E) separated by an energy gap (Δ), which is defined as positive if the singlet is the lowest level. Both perturbations must be considered simultaneously due to the strong spin-orbit coupling ($\lambda \approx -2000 \text{ cm}^{-1}$) and ligand field operating in the $5d$ metal ions, which results in six double-degenerated Kramer doublets, as shown in the splitting diagram in Figure 6 [9].

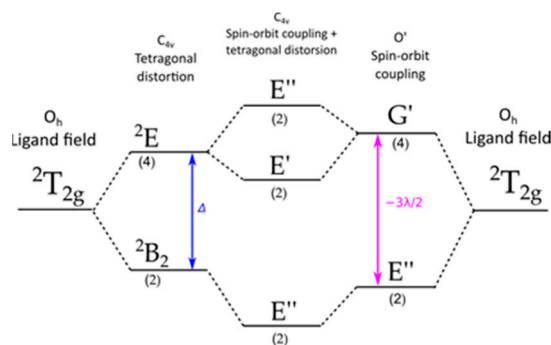


Figure 6. Splitting of the 2T_2 term by spin-orbit coupling and a tetragonal distortion. Numbers in parentheses correspond to the degree of orbital degeneracy.

The energy values associated with the wave functions of the 2T_2 term are calculated using the Figgis [49] and Mabbs [50] methodology. These values are the following: $E_1 = E_2 = \kappa\lambda(\nu - 0, 5)$, $E_3 = E_4 = \frac{\kappa\lambda}{\sqrt{2}}a$ and $E_5 = E_6 = \frac{\kappa\lambda}{\sqrt{2}}b$, ν being the tetragonal distortion parameter defined as $\nu = \Delta/\kappa\lambda$ with $a = \frac{1}{\sqrt{2}}[(\nu + 0, 5) - Z]$, $b = \frac{1}{\sqrt{2}}[(\nu + 0, 5) + Z]$ and $Z = \sqrt{\nu^2 + \nu + 2, 25}$. As the system is anisotropic, the effect of the magnetic field on the parallel direction (z) is different from that on the perpendicular ones (x and y). Under an axial symmetry, there is a parallel and a perpendicular component of the magnetic susceptibility [Equation (2)]:

$$\chi_{\parallel} = \frac{N_A\beta^2}{4kT} \left[\frac{2(\kappa + 1 - a^2)}{(1 + a^2)} \right]^2 - \frac{2N_A\beta^2(\kappa + 1 - ab)}{\kappa\lambda(1 + a^2)(1 + b^2)Z} \tag{2}$$

$$\chi_{\perp} = \frac{N_A\beta^2}{4kT} \left[\frac{2(\kappa a\sqrt{2} - a)}{(1 + a^2)} \right]^2 - \frac{2N_A\beta^2}{\kappa\lambda} \left\{ \frac{[k(a + b) - ab\sqrt{2}]^2}{2(1 + a^2)(1 + b^2)Z} - \frac{(\sqrt{2} - \kappa a)^2}{(1 + a^2)(\nu - 1, 5 - Z)} \right\}$$

Given that the magnetic susceptibility was measured on a powder sample, it must obey the expression $\chi_M = \frac{\chi_{\parallel} + 2\chi_{\perp}}{3}$. In the case where the intermolecular interactions are not considered, it is expected that a polycrystalline sample of any of the mononuclear Re(II) compounds would exhibit a Curie-law behavior with a total spin $S_{\text{eff}} = \frac{1}{2}$, ($\chi_M T = C = N\beta^2 g_{av}^2/4k$). If the temperature-independent paramagnetism is considered, the lineal equation $\chi_M T = A + BT$ is derived [Equations (3)–(5)]:

$$\chi_M T = N\beta^2 g_{av}^2/4k + \chi_{TIP}^{av} T \tag{3}$$

$$g_{av}^2 = (g_{\parallel}^2 + 2g_{\perp}^2)/3 \tag{4}$$

$$\chi_{TIP}^{av} = (\chi_{TIP}^{\parallel} + 2\chi_{TIP}^{\perp})/3 \quad (5)$$

The values of χ_{TIP}^u y g_u are deduced from Equation (2) and summarized in Table 2.

Table 2. Values of g and χ in the parallel and perpendicular directions to the magnetic field.

Direction (u)	g_u	χ_{TIP}^u
Parallel (z)	$\left[\frac{2(\kappa+1-a^2)}{(1+a^2)} \right]$	$-\frac{2N_A\beta^2(\kappa+1-ab)}{\kappa\lambda(1+a^2)(1+b^2)Z}$
Perpendicular (x and y)	$\left[\frac{2(\kappa a\sqrt{2}-a)}{(1+a^2)} \right]$	$-\frac{2N_A\beta^2}{\kappa\lambda} \left\{ \frac{[k(a+b)-ab\sqrt{2}]^2}{2(1+a^2)(1+b^2)Z} - \frac{(\sqrt{2}-\kappa a)^2}{(1+a^2)(v-1.5-Z)} \right\}$

It is worth mentioning that a Weiss constant θ (in the form of $T - \theta$) was introduced in the fitting procedure to account for the intermolecular magnetic interactions. The least-squares fit of the magnetic data using matrix-diagonalization techniques through the VPMAG [47] program led to the parameters listed in Table 3.

Table 3. Best-fit parameters for 1–4 ^a.

Compound	Δ	λ	κ	ν	TIP ^b	θ/K	g_{\parallel}	g_{\perp}	g_{av}	$R^c \times 10^6$
1	2225	−1847	0.62	−1.94	125	−1.78	1.25	2.33	2.03	0.5
2	2589	−1800	0.63	−2.28	98	−3.12	1.43	2.34	2.08	1.8
3	1850	−1899	0.63	−1.55	169	−0.59	1.01	2.32	1.98	0.2
4 ^d	2016	−1849	0.64	−1.70	155	−0.14	1.07	2.34	2.01	0.2

^a All energies are given in cm^{-1} . ^b $\chi_{TIP} = \text{TIP} \times 10^{-6} \text{ cm}^3 \text{ mol}^{-1}$ and calculated through Equations (2) and (3). ^c R is the agreement factor defined as $\sum[(\chi_{MT})_{\text{exp}} - (\chi_{MT})_{\text{calcd}}]^2 / \sum[(\chi_{MT})_{\text{exp}}]^2$. ^d Although there are two crystallographically non-equivalent $[\text{Re}(\text{NO})\text{Br}_4(\text{Htrz})]^-$ complex anions in **4**, they are structurally quite similar—in particular, the coordination geometry around the rhenium atom (Table 1); therefore, their magnetic behavior was assumed to be identical.

These values are similar to those previously obtained for other related Re(II)-nitrosyl complexes [9,10]. The relatively low values of κ (0.62 to 0.64) and high values of $|\lambda|$ (1800 to 1899 cm^{-1}) are indicative of a significant covalence degree of the rhenium to ligand interaction in 1–4. The value of Δ (axial distortion) is positive in sign, indicating that the orbital singlet (2B_2) is lower in energy than the doublet (2E) (Figure 6), in agreement with the electronic configuration expected for a tetragonal Re(II)-nitrosyl complex [51]. A simulation of the dependence of the g_u value with the distortion parameter ν by using the equations in Table 3, shown in Figure 7a, agrees with the experimental $g_{\parallel} < g_{\perp}$ pattern determined experimentally. Additionally, there is a good agreement between the experimental values calculated for the $g_{\parallel} < g_{\perp}$ pattern and those inferred from Figure 7b. ($g_{\perp} = 2.2 - 2.7$ and $g_{\parallel} = 0.9 - 1.4$), considering $\lambda = -2000 \text{ cm}^{-1}$ and values of κ in the range 0.5–0.75.

The calculated values of g and TIP are very close to those observed for similar complexes previously reported [9,10,14,52]. Finally, the exchange pathways for the very weak intermolecular magnetic interactions have to be attributed to the through-space Br \cdots Br, Br–H contacts, as well as π – π stacking interactions. Ligands that provide a supramolecular pathway through hydrogen bonding or halide–halide interactions may be essential for promoting significant magnetic interactions among mononuclear complexes in the crystal packing [52]. This is particularly relevant in the magnetochemistry of related mononuclear Re(IV) complexes (t_{2g}^3 electronic configuration), where through-space magnetic interactions can provide the magnetic pathways that lead to magnetic ordering at relatively high temperatures [53]. It is worth noting that although the shortest Br \cdots Br distances in **1** are close to the van der Waals one (ca. 3.7 Å) [42–44], they may still be viewed as likely magnetic exchange pathways.

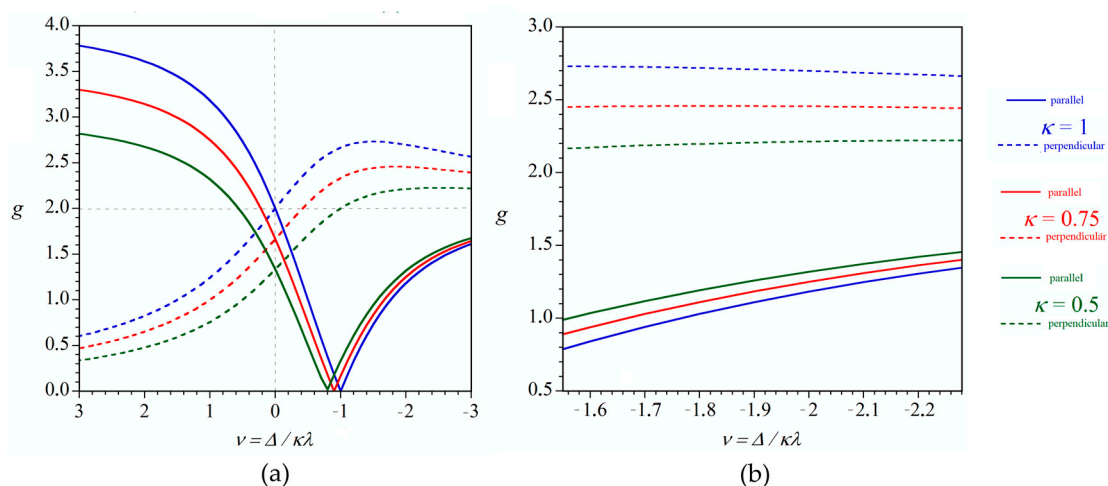


Figure 7. (a) Calculated values of the g factor for an electronic configuration t_2^5 ($\lambda < 0$) as a function of possible negative and positive values of the distortion factor (v) under different values of the covalence factor (κ). (b) Details of the calculated values of the g factor for $\lambda = -2000 \text{ cm}^{-1}$ and $\kappa = 0.5 - 0.75$.

4. Conclusions

Four mononuclear Re(II)-nitrosyl complexes with a series of azole-type molecules as co-ligands (compounds 1–4) were isolated and magnetostructurally investigated. A thorough analysis of the influence of the magnetic field, SOC, axial distortion, and covalence effects as variable parameters successfully simulated their cryomagnetic data. Very weak intermolecular antiferromagnetic interactions occur in 1–4, the through-space Br \cdots Br contacts, among other weak intermolecular interactions, providing exchange pathways for these complexes. The use of Hirshfeld surface analysis in the solid-state structure studies of 1–4 enabled the visualization of the proportion and nature of the interactions present in the structures, some of which are not immediately evident through knowledge of the crystal structure alone. Determining these intrinsic parameters and their relation to molecular or crystal structure is critical in providing essential tools for the rational design of molecular materials with interesting magnetic properties.

Supplementary Materials: The following supporting information can be downloaded at: <https://www.mdpi.com/article/10.3390/cryst13040658/s1>, Table S1. List of the infrared absorption bands observed in compounds 1–4, and classified upon their origin. (ligand, NBu_4^+ or Re-NO). Table S2. Summary of the crystal data and structure refinement for 1–4. Table S3. Geometrical distortion from OC-6 calculated by CSM (OC-6) and the calculated tetragonal distortion for several tetrabromonitrosylrhenium(II) complexes. Figure S1. (a) Packing diagram down the crystallographic a axis, (b) fingerprint plot, (c) d_{norm} surface, and (d) shape index surface of the $[\text{Re}(\text{NO})\text{Br}_4(\text{Hpz})]^-$ anionic units in 2. Short Br \cdots Br (yellow dashed lines) contacts and π - π stacking interactions (grey ovals) are shown. Figure S2. (a) Packing diagram down the crystallographic a axis, (b) fingerprint plot, (c) d_{norm} surface, and (d) shape index surface of the $[\text{Re}(\text{NO})\text{Br}_4(\text{Htz})]^-$ anionic units in 3. Short Br \cdots Br (yellow), Br \cdots H (red) contacts and π - π stacking interactions (grey ovals) are shown. File S1. checkCIF/PLATON report.

Author Contributions: M.P.: Methodology, Investigation, Formal analysis, Writing—original Draft, review and Editing, Visualization. J.G.-P.: Investigation, Formal analysis, Resources, Writing—Review. C.K.: Conceptualization. M.J.: Formal analysis, Visualization, Writing—Original Draft, review and Editing, Resources. F.L.: Formal analysis, Visualization, Writing—Original Draft, Review and Editing, Resources. A.C.: Conceptualization, Supervision, Writing—Review, Project administration. All authors have read and agreed to the published version of the manuscript.

Funding: Financial support from PEDECIBA (Uruguay), CSIC (Uruguay, Programa de Apoyo a Grupos de Investigación, Project N°245), MICIU (Spain, Project PID2019-109735GB-I00), the Generalitat Valenciana (Spain, AICO/2020/183 and AICO/2021/295), Agencia Estatal de Investigación under the National Program of Sciences and Technological Materials (Spain, PID2019-106383GB-C44/AEI/10.13039/501100011033) and by EU-FEDER is gratefully acknowledged.

Institutional Review Board Statement: Not applicable.

Informed Consent Statement: Not applicable.

Data Availability Statement: No data provided.

Acknowledgments: M.P. thanks Fundación Carolina (ES), CAP-UdelaR (UY) and ANII (UY) for studentship grants. J.G.-P. thanks to Servicios Generales de Apoyo a la Investigación (SEGAI) at La Laguna University.

Conflicts of Interest: The authors declare no conflict of interest. The funders had no role in the design of the study; in the collection, analyses, or interpretation of data; in the writing of the manuscript; or in the decision to publish the results.

References

1. Dudle, B.; Rajesh, K.; Blacque, O.; Berke, H. Rhenium in Homogeneous Catalysis: [ReBrH(NO)(Labile Ligand)(Large-Bite-Angle Diphosphine)] Complexes as Highly Active Catalysts in Olefin Hydrogenations. *J. Am. Chem. Soc.* **2011**, *133*, 8168–8178. [[CrossRef](#)] [[PubMed](#)]
2. Jiang, Y.; Blacque, O.; Berke, H. Probing the Catalytic Potential of Chloro Nitrosyl Rhenium(I) Complexes. *Dalton Trans.* **2011**, *40*, 2578–2587. [[CrossRef](#)]
3. Zobi, F.; Blacque, O. Reactivity of 17 E – Complex [ReIIBr₄(CO)₂]²⁻ with Bridging Aromatic Ligands. Characterization and CO-Releasing Properties. *Dalton Trans.* **2011**, *40*, 4994–5001. [[CrossRef](#)]
4. Adams, J.J.; Arulsamy, N.; Sullivan, B.P.; Roddick, D.M.; Neuberger, A.; Schmehl, R.H. Homoleptic Tris-Diphosphine Re(I) and Re(II) Complexes and Re(II) Photophysics and Photochemistry. *Inorg. Chem.* **2015**, *54*, 11136–11149. [[CrossRef](#)]
5. Bar, A.K.; Pichon, C.; Sutter, J.-P. Magnetic Anisotropy in Two- to Eight-Coordinated Transition-Metal Complexes: Recent Developments in Molecular Magnetism. *Coord. Chem. Rev.* **2016**, *308*, 346–380. [[CrossRef](#)]
6. Wang, X.-Y.; Avendaño, C.; Dunbar, K.R. Molecular Magnetic Materials Based on 4d and 5d Transition Metals. *Chem. Soc. Rev.* **2011**, *40*, 3213–3238. [[CrossRef](#)] [[PubMed](#)]
7. Schelter, E.J.; Prosvirin, A.V.; Dunbar, K.R. Molecular Cube of ReII and MnII That Exhibits Single-Molecule Magnetism. *J. Am. Chem. Soc.* **2004**, *126*, 15004–15005. [[CrossRef](#)] [[PubMed](#)]
8. Schelter, E.J.; Prosvirin, A.V.; Reiff, W.M.; Dunbar, K.R. Unusual Magnetic Metal–Cyanide Cubes of ReII with Alternating Octahedral and Tetrahedral Corners. *Angew. Chem. Int. Ed.* **2004**, *43*, 4912–4915. [[CrossRef](#)]
9. Pacheco, M.; Cuevas, A.; González-Platas, J.; Faccio, R.; Lloret, F.; Julve, M.; Kremer, C. Synthesis, Crystal Structure and Magnetic Properties of the Re(II) Complexes NBu₄[Re(NO)Br₄(L)] (L = Pyridine and Diazine Type Ligands). *Dalton Trans.* **2013**, *42*, 15361–15371. [[CrossRef](#)]
10. Pacheco, M.; Cuevas, A.; González-Platas, J.; Lloret, F.; Julve, M.; Kremer, C. The Crystal Structure and Magnetic Properties of 3-Pyridinecarboxylate-Bridged Re(ii)M(ii) Complexes (M = Cu, Ni, Co and Mn). *Dalton Trans.* **2015**, *44*, 11636–11648. [[CrossRef](#)] [[PubMed](#)]
11. Pacheco, M.; González-Platas, J.; Julve, M.; Lloret, F.; Kremer, C.; Cuevas, A. Crystal Structure and Magnetic Properties of 3,5-Pyridinedicarboxylate-Bridged Re(II)M(II) Heterodinuclear Complexes (M = Cu, Ni and Co). *Polyhedron* **2021**, *208*, 115414. [[CrossRef](#)]
12. Rosas, K.S.; Torres, J.; Pacheco, M.; Ramos, J.; Gancheff, J.S. Proton-Transfer Reactions of Re(II)-Nitrosyl Complexes: Potentiometric Studies, DFT and TD-DFT Calculations. *Results Chem.* **2022**, *4*, 100455. [[CrossRef](#)]
13. Pacheco, M.; Cuevas, A.; González-Platas, J.; Gancheff, J.S.; Kremer, C. Complex Salts of [Re^{II}(NO)Br₄(Pyz)]⁻: Synthesis, Crystal Structures, and DFT Studies. *J. Coord. Chem.* **2014**, *67*, 4028–4038. [[CrossRef](#)]
14. Pacheco, M.; Alvarez, N.; Cuevas, A.; Romerosa, A.; Lloret, F.; Kremer, C. Crystal Structure and Magnetic Study of the Complex Salt [RuCp(PTA)₂-μ-CN-1κC:2κN-RuCp(PTA)₂][Re(NO)Br₄(EtOH)_{0.5}(MeOH)_{0.5}]. *Acta Crystallogr. Sect. E Crystallogr. Commun.* **2021**, *77*, 749–754. [[CrossRef](#)]
15. Pacheco, M.; Cuevas, A.; González-Platas, J.; Kremer, C. Synthesis, Spectroscopic Characterization and Crystal Structure of [ReV(O)₂(Pyz)₄][ReII(NO)Br₄(Pyz)] (Pyz = Pyrazine). *Commun. Inorg. Synth.* **2015**, *2*, 20–24. [[CrossRef](#)]
16. Kahn, O. *Molecular Magnetism*; Wiley-VCH: New York, NY, USA, 2001; ISBN 978-0-471-18838-4.
17. Barbour, L.J. Single-Crystal X-ray Diffraction. In *Comprehensive Supramolecular Chemistry II*; Elsevier: Amsterdam, The Netherlands, 2017; pp. 23–43. ISBN 978-0-12-803199-5.
18. McKinnon, J.J.; Jayatilaka, D.; Spackman, M.A. Towards Quantitative Analysis of Intermolecular Interactions with Hirshfeld Surfaces. *Chem. Commun.* **2007**, *7*, 3814–3816. [[CrossRef](#)]

19. Aromí, G.; Barrios, L.A.; Roubeau, O.; Gamez, P. Triazoles and Tetrazoles: Prime Ligands to Generate Remarkable Coordination Materials. *Coord. Chem. Rev.* **2011**, *255*, 485–546. [CrossRef]
20. Chen, S.-S. The Roles of Imidazole Ligands in Coordination Supramolecular Systems. *Crystengcomm* **2016**, *18*, 6543–6565. [CrossRef]
21. Haasnoot, J.G. Mononuclear, Oligonuclear and Polynuclear Metal Coordination Compounds with 1,2,4-Triazole Derivatives as Ligands. *Coord. Chem. Rev.* **2000**, *200–202*, 131–185. [CrossRef]
22. Li, H.; Zhang, S.-G.; Xie, L.-M.; Yu, L.; Shi, J.-M. π - π Stacking, Hydrogen Bonding and Anti-Ferromagnetic Coupling Mechanism on a Mononuclear Cu(II) Complex. *J. Coord. Chem.* **2011**, *64*, 1456–1468. [CrossRef]
23. Earnshaw, A. *Introduction to Magnetochemistry*; Elsevier Science: Saint Louis, MI, USA, 2013; ISBN 978-1-4832-7069-2.
24. AIST: Spectral Database for Organic Compounds, SDDBS. Available online: http://sdbs.db.aist.go.jp/sdbs/cgi-bin/cre_index.cgi (accessed on 15 October 2016).
25. Nakamoto, K. Complexes of Alcoxides, Alcohols, Ethers, Ketones, Aldehydes, Esteres, and Carboxylic Acids. En: *Infrared and Raman Spectra of Inorganic and Coordination Compounds. In Part II: Applications in Coordination, Organometallic, and Bioinorganic*; John Wiley & Sons: Hoboken, NJ, USA, 1997.
26. Billes, F.; Endrédi, H.; Keresztury, G. Vibrational Spectroscopy of Triazoles and Tetrazole. *J. Mol. Struct. THEOCHEM* **2000**, *530*, 183–200. [CrossRef]
27. Agilent Technologies. CrysAlisPro (v42). Agilent Technologies, Oxfordshire, UK. 2021. Available online: <https://www.rigaku.com/products/crystallography/crysalis> (accessed on 6 April 2023).
28. BRUKER APEX2. Available online: <https://www.cif.iastate.edu/x-ray/apexii> (accessed on 3 April 2023).
29. Palatinus, L.; Chapuis, G. Superflip—A Computer Program for the Solution of Crystal Structures by Charge Flipping in Arbitrary Dimensions. *J. Appl. Crystallogr.* **2007**, *40*, 786–790. [CrossRef]
30. Sheldrick, G.M. Crystal Structure Refinement with SHELXL. *Acta Cryst. C* **2015**, *71*, 3–8. [CrossRef]
31. Speck, A. *Platon: A Multipurpose Crystallographic Tool*; Utrecht University: Utrecht, The Netherlands, 2002.
32. Dolomanov, O.V.; Bourhis, L.J.; Gildea, R.J.; Howard, J.A.K.; Puschmann, H. OLEX2: A Complete Structure Solution, Refinement and Analysis Program. *J. Appl. Crystallogr.* **2009**, *42*, 339–341. [CrossRef]
33. Macrae, C.F.; Sovago, I.; Cottrell, S.J.; Galek, P.T.A.; McCabe, P.; Pidcock, E.; Platings, M.; Shields, G.P.; Stevens, J.S.; Towler, M.; et al. Mercury 4.0: From Visualization to Analysis, Design and Prediction. *J. Appl. Crystallogr.* **2020**, *53*, 226–235. [CrossRef] [PubMed]
34. Spackman, M.A.; Jayatilaka, D. Hirshfeld Surface Analysis. *CrystEngComm* **2009**, *11*, 19–32. [CrossRef]
35. Turner, M.J.; McKinnon, J.J.; Wolff, S.K.; Grimwood, D.J.; Spackman, P.R.; Jayatilaka, D.; Spackman, M.A. *CrystalExplorer17*; University of Western Australia: Perth, Australia, 2017.
36. Spackman, M.A.; McKinnon, J.J. Fingerprinting Intermolecular Interactions in Molecular Crystals. *CrystEngComm* **2002**, *4*, 378–392. [CrossRef]
37. McKinnon, J.J.; Spackman, M.A.; Mitchell, A.S. Novel Tools for Visualizing and Exploring Intermolecular Interactions in Molecular Crystals. *Acta Crystallogr. Sect. B Struct. Sci.* **2004**, *60*, 627–668. [CrossRef]
38. Ciani, G.; Giusto, D.; Manassero, M.; Sansoni, M. Reactions of Pentachloro- and Pentabromonitrosylrhene(II) Anions with N-Donor Ligands. *Gazz. Chim. Ital.* **1977**, *107*, 429–430.
39. Steed, J.W.; Atwood, J.L. *Supramolecular Chemistry*, 2nd ed.; Wiley: Chichester, UK, 2009; ISBN 978-0-470-51233-3.
40. Alkorta, I.; Elguero, J.; Frontera, A. Not Only Hydrogen Bonds: Other Noncovalent Interactions. *Crystals* **2020**, *10*, 180. [CrossRef]
41. Cuevas, A.; Chiozzzone, R.; Kremer, C.; Suescun, L.; Mombrú, A.; Armentano, D.; De Munno, G.; Lloret, F.; Cano, J.; Faus, J. Rhenium (IV)-Copper (II) Heterobimetallic Complexes with a Bridge Malonato Ligand. Synthesis, Crystal Structure, and Magnetic Properties. *Inorg. Chim. Acta* **2004**, *43*, 7823–7831. [CrossRef] [PubMed]
42. Cuevas, A.; Kremer, C.; Hummert, M.; Schumann, H.; Lloret, F.; Julve, M.; Faus, J. Magnetic Properties and Molecular Structures of Binuclear (2-Pyrazinecarboxylate)-Bridged Complexes Containing Re (IV) and M (II)(M = Co, Ni). *Dalton Trans.* **2007**, *3*, 342–350. [CrossRef] [PubMed]
43. Martínez-Lillo, J.; Armentano, D.; Munno, G.D.; Julve, M.; Lloret, F.; Faus, J. Ferromagnetic Coupling and Spin Canting Behaviour in Heterobimetallic ReIVMII/III (M = CoII/III, NiII) Species. *Dalton Trans.* **2013**, *42*, 1687–1695. [CrossRef]
44. Schiemenz, G.P. The Sum of van der Waals Radii—A Pitfall in the Search for Bonding. *Z. Für Nat. B* **2007**, *62*, 235–243. [CrossRef]
45. Tan, S.L.; Jotani, M.M.; Tiekink, E.R.T. Utilizing Hirshfeld Surface Calculations, Non-Covalent Interaction (NCI) Plots and the Calculation of Interaction Energies in the Analysis of Molecular Packing. *Acta Crystallogr. Sect. E Cryst. Commun.* **2019**, *75*, 308–318. [CrossRef] [PubMed]
46. Lloret, F.; Julve, M.; Cano, J.; Ruiz-García, R.; Pardo, E. Magnetic Properties of Six-Coordinated High-Spin Cobalt(II) Complexes: Theoretical Background and Its Application. *Inorg. Chim. Acta* **2008**, *361*, 3432–3445. [CrossRef]
47. Machura, B. Structural and Spectroscopic Properties of Rhenium Nitrosyl Complexes. *Coord. Chem. Rev.* **2005**, *249*, 2277–2307. [CrossRef]
48. Figgis, B.N. The Magnetic Properties of Transition Metal Ions in Asymmetric Ligand Fields. Part 3.—The Behaviour of Some T52g Complexes. *Trans. Faraday Soc.* **1961**, *57*, 204–209. [CrossRef]
49. Mabbs, F.E.; Machin, D.J. *Magnetism and Transition Metal Complexes*; Springer: Berlin/Heidelberg, Germany, 1973; ISBN 978-1-5041-2035-7.

50. Cano, J. *VPMAG*; University of Valencia: Valencia, Spain, 2003.
51. Schelter, E.J.; Bera, J.K.; Bacsa, J.; Galán-Mascarós, J.R.; Dunbar, K.R. New Paramagnetic Re(II) Compounds with Nitrile and Cyanide Ligands Prepared by Homolytic Scission of Dirhenium Complexes. *Inorg. Chem.* **2003**, *42*, 4256–4258. [[CrossRef](#)]
52. Silva, C.P.; Junior, H.C.S.; Santos, I.F.; Bernardino, A.M.R.; Cassaro, R.A.A.; Novak, M.A.; Vaz, M.G.F.; Guedes, G.P. Synthesis, Crystal Structure, Magnetic Properties and DFT Calculations of a Mononuclear Copper(II) Complex: Relevance of Halogen Bonding for Magnetic Interaction. *Inorg. Chim. Acta* **2018**, *482*, 395–401. [[CrossRef](#)]
53. Martínez-Lillo, J.; Faus, J.; Lloret, F.; Julve, M. Towards multifunctional magnetic systems through molecular-programmed self assembly of Re(IV) metalloligands. *Coord. Chem. Rev.* **2015**, *289–290*, 215–237. [[CrossRef](#)]

Disclaimer/Publisher's Note: The statements, opinions and data contained in all publications are solely those of the individual author(s) and contributor(s) and not of MDPI and/or the editor(s). MDPI and/or the editor(s) disclaim responsibility for any injury to people or property resulting from any ideas, methods, instructions or products referred to in the content.